

Design and properties of a cryogenic dip-stick scanning tunneling microscope with capacitive coarse approach control

R. Schlegel, T. Hänke, D. Baumann, M. Kaiser, P. K. Nag, R. Voigtländer, D. Lindackers, B. Büchner, and C. Hess

Citation: [Review of Scientific Instruments](#) **85**, 013706 (2014); doi: 10.1063/1.4862817

View online: <http://dx.doi.org/10.1063/1.4862817>

View Table of Contents: <http://scitation.aip.org/content/aip/journal/rsi/85/1?ver=pdfcov>

Published by the [AIP Publishing](#)

Articles you may be interested in

[Atomic resolution ultrafast scanning tunneling microscope with scan rate breaking the resonant frequency of a quartz tuning fork resonator](#)

Rev. Sci. Instrum. **82**, 053705 (2011); 10.1063/1.3585200

[Scanning tunneling microscope with two-dimensional translator](#)

Rev. Sci. Instrum. **82**, 013706 (2011); 10.1063/1.3548832

[A cryogenic Quadraprobe scanning tunneling microscope system with fabrication capability for nanotransport research](#)

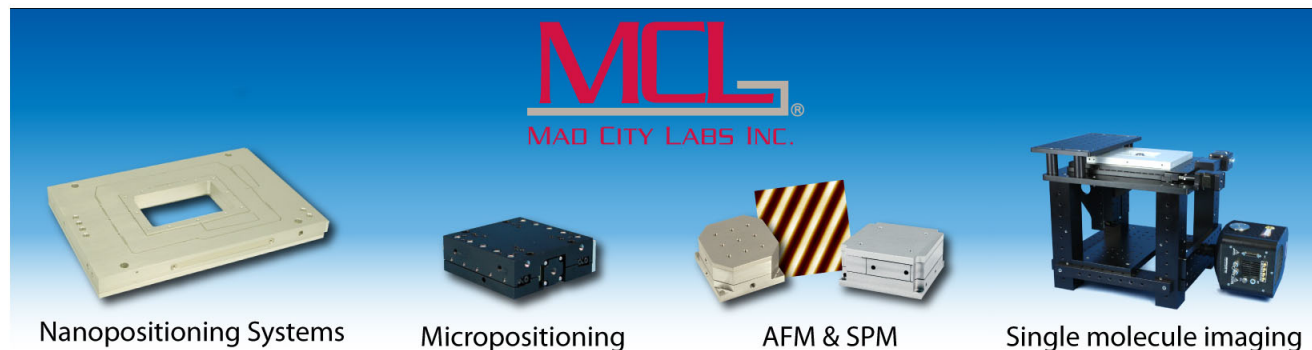
Rev. Sci. Instrum. **78**, 123701 (2007); 10.1063/1.2821610

[Cryogenic variable temperature ultrahigh vacuum scanning tunneling microscope for single molecule studies on silicon surfaces](#)

Rev. Sci. Instrum. **75**, 5280 (2004); 10.1063/1.1818871

[A simple scanning tunneling microscope](#)

Am. J. Phys. **65**, 160 (1997); 10.1119/1.18504



Design and properties of a cryogenic dip-stick scanning tunneling microscope with capacitive coarse approach control

R. Schlegel,^{1,a)} T. Hänke,¹ D. Baumann,¹ M. Kaiser,¹ P. K. Nag,¹ R. Voigtländer,¹ D. Lindackers,¹ B. Büchner,^{1,2} and C. Hess^{1,2,b)}

¹Leibniz-Institute for Solid State and Materials Research, IFW-Dresden, 01171 Dresden, Germany

²Center for Transport and Devices, Technische Universität Dresden, 01069 Dresden, Germany

(Received 17 October 2013; accepted 7 January 2014; published online 29 January 2014)

We present the design, setup, and operation of a new dip-stick scanning tunneling microscope. Its special design allows measurements in the temperature range from 4.7 K up to room temperature, where cryogenic vacuum conditions are maintained during the measurement. The system fits into every ⁴He vessel with a bore of 50 mm, e.g., a transport dewar or a magnet bath cryostat. The microscope is equipped with a cleaving mechanism for cleaving single crystals in the whole temperature range and under cryogenic vacuum conditions. For the tip approach, a capacitive automated coarse approach is implemented. We present test measurements on the charge density wave system 2H-NbSe₂ and the superconductor LiFeAs which demonstrate scanning tunneling microscopy and spectroscopy data acquisition with high stability, high spatial resolution at variable temperatures and in high magnetic fields. © 2014 AIP Publishing LLC. [<http://dx.doi.org/10.1063/1.4862817>]

I. INTRODUCTION

In recent years, scanning tunneling microscopy and spectroscopy (STM/STS) at low temperatures has become of increasing importance in condensed matter physics. Prominent examples are spectroscopic imaging investigations of quasiparticle interference in metals,^{1,2} unconventional superconductors,^{3–6} and topological insulators,^{7,8} or single atom manipulation and spectroscopy including spin resolution.^{9–12} Such investigations require, apart from low temperature and high stability measurement conditions, the maintenance of ultra-high-vacuum (UHV) and means of preparing clean surfaces in UHV. A typical approach is to implement the STM into a specialized UHV setup and to apply UHV compatible techniques for surface preparation, i.e., applying sputtering and annealing cycles¹³ and *in situ* growth of thin films.^{14,15} These techniques, however, are well feasible only for non-complex elementary or at most binary materials. The preparation of clean crystal surfaces in the case of more complex compounds therefore requires a different approach, namely cleaving a single crystal of the compound in the vacuum chamber.

The implementation of a cryogenic STM into an UHV chamber is a rather challenging task because several obstacles have to be overcome. Most crucial is that the operation of a cryogenic STM in an UHV chamber, which normally is at room temperature, requires a sophisticated thermal shielding setup. Furthermore, the pressure inside the STM chamber must be very low in order to prevent the cold sample surface to act as a getter for residual gases. Technical solutions which fulfil these criteria tend to be complex and bear the risk of fatal errors of the operator which could lead to loss of the sample and in worst case of the setup.

The aim for our work which is presented in this paper was to circumvent these difficulties and to develop a cryogenic STM with a minimum of technical complexity. Our design which waives any UHV chamber is based on a STM which is mounted in a vacuum tube. Upon immersing the evacuated tube into a bath of liquid ⁴He, a cryogenic vacuum is created at the STM which is simultaneously cooled to a temperature close to that of the bath. Perfectly clean single crystal surfaces for STM measurements can afterwards be prepared by a mechanism for cleaving samples inside the STM at cryogenic vacuum conditions. The diameter of the vacuum tube is rather small which allows to operate the STM in any ⁴He vessel, including commercial magnet bath cryostats, which opens up the possibility to perform STM/STS measurements in high magnetic fields. Special attention is given to the problem of approaching the STM tip towards the sample because the system lacks any optical control once it is inserted in the He-bath. We describe a capacitive coarse approach technique which performs an automated tip approach over a distance of ~20 mm in less than 2 h. Results of test measurements on 2H-NbSe₂ and LiFeAs at various temperatures and in magnetic field are presented which demonstrate the outstanding capabilities of this STM system.

II. INSTRUMENT DESIGN

The STM system is based on a tube design (Figure 1) that waives the frequently used UHV chamber in cryogenic STM. The outer shell is formed by a stainless steel tube (A) and the upper part (B) which are connected via a KF50 flange connection. The latter hosts the pump port, electrical feedthroughs, and parts for operating a sample cleaving mechanism (see below). The inner part comprises the radiation baffle structure (C), on which the thermal coupling (D) and the STM head (E) are suspended. The thermal coupling is the only part of the cryogenic section which possesses a direct thermal

^{a)}Electronic mail: R.Schlegel@ifw-dresden.de

^{b)}Electronic mail: C.Hess@ifw-dresden.de

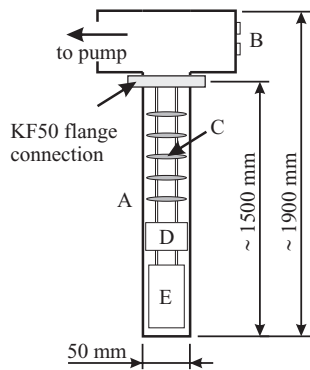


FIG. 1. Scheme of the STM system: (A) stainless steel tube, (B) electrical feedthroughs and pump port, (C) radiation baffle structure, (D) thermal coupling, and (E) STM head. After mounting the sample in the STM head, the inner part is inserted into the stainless steel tube which is connected to the upper part by a KF50 clamp.

connection to the tube A. For operating the system it needs to be evacuated to a maximum pressure of 10^{-5} mbar prior to inserting it in to a bath of liquid ^4He . The outer diameter of the tube A of 50 mm renders the system compatible with standard ^4He transport dewars and magnet cryostats with a corresponding bore size. Once immersed in the liquid helium bath, a cryogenic vacuum is formed ($p \lesssim 10^{-10}$ mbar¹⁶) inside the tube and the STM head (E) is cooled down to the system's base temperature of ~ 5 K. The system contains a mechanism for cleaving samples inside the STM head at cryogenic vacuum conditions.

A. External vibration insulation

For the damping of external mechanical noise we employ a two-step damping system as illustrated in Figure 2. The dewar (item 4 in Figure 2) (alternatively, the magnet cryostat, maximum weight: 500 kg, maximum outer diameter: 1 m) which hosts the STM system (5) is suspended from the frame (I, II, III) with three heavy duty straps (3). The frame (I, II, III) is divided into three sub-frames. The first sub frame (I, diamonds) brings the other two sub-frames to the necessary height that the dewar can be lifted from above. The second sub-frame (II, crossed lines) is mounted on four air compact cylinders¹⁷ (1) for lifting the dewar. Sub-frame (II) carries the damping system¹⁸ (2).

Sub frame (III, diagonal lines) rests on the damping stage (2) and carries the mounting parts for the heavy duty straps (3). After attaching the dewar to the straps (3), the dewar is brought to levitation by extending the compact cylinders. The air springs (2) and the compact cylinders (1) are operated at 6 bar compressed air.

The combination of air springs and straps results in a vertical vibration resonance frequency of the dewar center of mass of ~ 4.5 Hz. In combination with the eigenfrequency of the scanner tube ($f_{\text{scanner}} \approx 4$ kHz) this yields a sufficient insulation against floor vibrations.

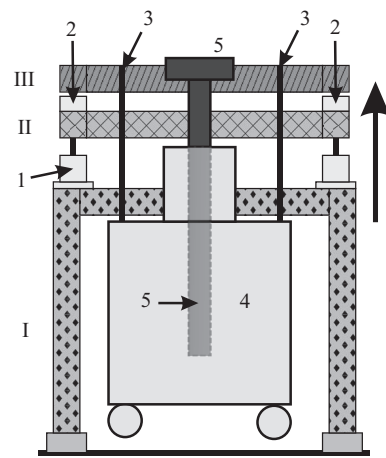


FIG. 2. Schematic diagram of the STM system in a dewar mounted to the damping frame. The frame is divided in three sub frames for the purpose of supporting (I, diamonds), lifting (II, crossed lines), and damping (III, diagonal lines): (1) air compact cylinders for lifting, (2) air springs, (3) heavy duty straps, (4) ^4He -dewar, and (5) STM system.

B. General design of the dip-stick-STM

Figure 3 depicts a more detailed view on the general design of the STM system. The top part consists of the sample cleaving mechanism control (item 1 in Figure 3) and the connections for electrical wiring and pumping (2). The cleaving mechanism itself is a rotary feedthrough with a winch mounted at the vacuum side. By turning the rotary feedthrough, the cleaving wire is rolled up which results in a pulling force at the cleaving stamp on the sample (see Sec. II D). The electrical feedthroughs contain heater and temperature connections, high-voltage connections for the scanner tube, and the coarse approach motor as well as the

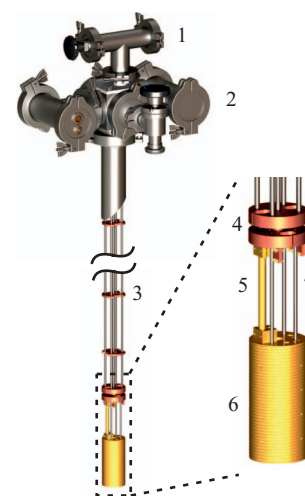


FIG. 3. Design of the STM system with a section through the stainless steel tube. The middle part has been cut out for better visualization. The image magnification shows the cold section with the heater cup attached to the STM head. (1) Cleaving mechanism control, (2) connections for electrical wiring and pumping, (3) stainless steel capillary tubes with heat radiation baffles, (4) copper disks for thermal coupling to the helium reservoir, (5) thermal connection to the STM head, (6) STM head with heating cup, and (7) stainless steel capillary tubes.

connections for sample bias voltage V_{bias} and tunneling current I_T .

The baffle structure provides a sufficient shielding of thermal intake in the form of radiation and heat conduction at the cold parts of the system. It consists of stainless steel capillary tubes (7) which minimize the heat conduction and provide the sufficient mechanical stiffness. The actual baffles (3) are circular copper plates with notches on two opposite sides which provide large enough cross section for pumping the system and wiring. Adjacent baffles are rotated by 90° against each other to avoid direct heat radiation to the cold parts. All wires connecting the feedthroughs and the STM are thermally anchored at the heat radiation baffles for further reducing the heat load.

The cold section comprises of the thermal coupling (4) and the STM head (6). The thermal coupling consists of two massive copper disks which fit to the inner diameter of the outer tube and thus provide a good thermal connection towards the ^4He bath. The STM head is connected to the thermal coupling via four stainless steel capillaries (7). In order to adjust the thermal conductance between both, an additional thermal connection (5), e.g., a massive copper rod or a copper braid may be installed. The whole STM head is covered by a heating cup (6). This cup allows to heat the STM head and, by compensating the cooling through the thermal coupling, to stabilize any temperature between base temperature and 300 K.

C. Design and properties of the STM head

The home-built STM head (Figure 4) is based on a design by Pan²¹ which has been modified to allow *in situ* cleaving. The body of the STM head, including the sample holder section and the top plate where the heating cup and the stainless steel capillary tubes are attached, is fabricated of gold-plated phosphor bronze. All assembled parts of the STM head have been made of non-magnetic materials in order to minimize magnetic stray fields at the sample and unwanted forces due to external magnetic field gradients.

The major part inside the STM head is the scanner unit consisting of a sapphire prism (11), the tube scanner holder (10), and the tube scanner (15) which is mounted inside of the prism. The scanner tube is a five-electrode piezoelectric tube²² with the four x/y -electrode segments on the outside and the z -electrode on the inside. At 300 K (6 K) the range of the tube scanner is $2.0\ \mu\text{m}$ (600 nm) and $1.4\ \mu\text{m}$ (260 nm) for the x/y and z directions, respectively.

A Macor socket with a molybdenum spring is installed on the end of the scanner tube which allows an easy exchange of the tip holder (16).

The scanner unit is clamped inside the STM body by six piezoelectric walker stacks (13) for the coarse approach motor. These stacks have been assembled using conductive glue.²³ A polished Al_2O_3 plate forms the interface between the piezoelectric stacks and the sapphire prism. Four of the stacks are attached directly to the STM body whereas the remaining two are glued onto a counterpart plate (12), again using Epotek H20E.²³ The counterpart plate is pressed against

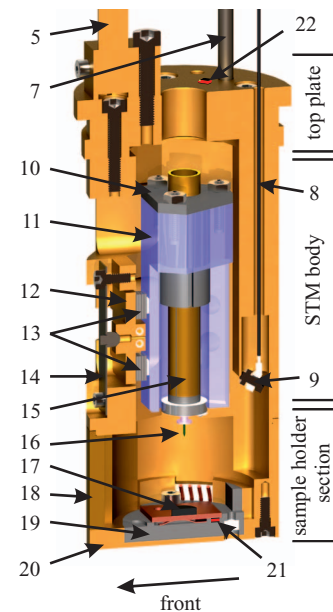


FIG. 4. Schematic section of the STM head which can be divided into three sections: top plate, STM body, and sample holder section: (5) thermal connection, (7) stainless steel capillary tube, (8) cleaving wire, (9) cleaving stamp, (10) tube scanner holder (Macor),¹⁹ (11) sapphire prism, (12) counterpart plate, (13) shear-piezo stacks, (14) molybdenum leaf spring, (15) tube scanner, (16) tip holder with tip, (17) sample, (18) front panel, (19) Macor part for bias insulation, (20) bottom plate, (21) Cernox²⁰ sample temperature sensor, and (22) Cernox STM body temperature sensor.

the sapphire prism by a molybdenum spring (14). By changing the spring force with a screw, it is possible to adjust the friction between the sapphire prism and the Al_2O_3 plates. With optimized spring force, it is possible to achieve a reliable scanner movement in the whole temperature range of the STM. The coarse approach motor itself has a maximum travel distance of 20 mm and the chosen mode of operation is the slip-stick-method.²⁴ For the coarse approach step width we estimated 250 nm (75 nm) at 300 K (6 K).

For easy sample mounting, the sample holder section is modularly designed. It consists of the bottom plate (20) and the front panel (18). The sample is mounted on a Macor part (19) on the bottom plate which electrically insulates the sample bias voltage and the ground. The front panel and the bottom plate are attached by titanium screws and can be removed for the sample mounting.

Two Cernox resistive thermometers²⁰ are mounted on the STM head. They are located at the top plate (22) and in the sample holder section (21) in direct vicinity of the sample.

On the vacuum side, UHV compatible coaxial wires have been used for V_{bias} and I_T . V_{bias} is connected to the sample while I_T is measured on the tip. All other wires used on the vacuum side are made of twisted pairs of polyimide-coated wires.

D. Sample mounting and cleaving

Prior to each measurement on a sample, it has to be glued onto a metallic sample holder with a conductive glue.²³ In order to create and to maintain a perfectly clean sample surface for STM measurements, it is indispensable to prepare the

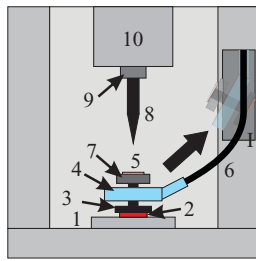


FIG. 5. Scheme of a prepared and mounted sample. The movement of the cleaving stamp during the cleaving procedure is indicated by the broad arrow. (1) Sample holder, (2) sample, (3) cleaving post with a screw thread on one end, (4) insulating eye, (5) test sample (e.g., gold on mica), (6) cleaving wire, (7) screw nut, (8) tip, (9) tip holder, (10) scanner unit, (I) parking position of the cleaving stamp. The insulating eye is made of copper and soldered to the cleaving wire. A coating of Epotek H70E²⁵ insulating glue prevents short-circuiting V_{bias} and ground.

sample surface under cryogenic vacuum conditions. Therefore, an *in situ* cleaving mechanism has been implemented. Figure 5 shows a scheme of the cleaving setup used in our system. As can be seen in Figure 5, a metallic cleaving post (3) is glued on top of the sample (2). The sample holder (1) is fastened on the Macor part in the sample holder section (item (19) in Fig. 4). Afterwards, the insulating eye (4) which is attached to the cleaving wire (6) is mounted with a screw nut (7) on top of the cleaving post. It is possible to mount a test sample (5) on top of the screw nut which provides the option to characterize and optimize the STM tip (e.g., by field emission²⁶) prior to the cleaving of the actual sample (2).

For the test measurement, the same electrical connections for V_{bias} and I_T are used as in the actual STM measurement. This is possible if both the sample (2) and the cleaving post (3) possess a sufficient electrical conductance. At the same time electrical short-circuiting of the bias voltage to the ground must be prevented (cf. Fig. 6 for an electric wiring scheme), which is achieved by the usage of the insulating eye (4) between the cleaving post (3) and the cleaving wire (6).

For cleaving the sample, the tip has to be fully retracted with the coarse approach motor to avoid tip damage during the cleaving process. By turning the rotary feedthrough (item (1) in Fig. 3), the wire (6) pulls away the cleaving post (3) which cleaves the sample. The post is then pulled into the parking position indicated in Figure 5, where it rests during the entire measurement.

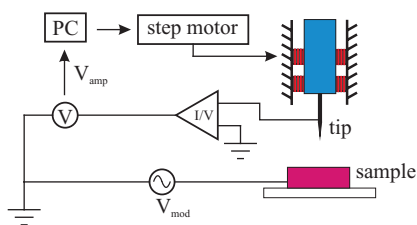


FIG. 6. Automatization scheme of the coarse approach. The modulation V_{mod} is applied to the sample bias V_{bias} . V_{amp} is the response signal which is measured by the tunnel current amplifier and a voltmeter. A computer program calculates the voltage differences ΔV and the second derivative and uses these results to control the coarse approach step motor.

E. External instrumentation

In order to achieve reliable results with the STM system, we use additional commercially available equipment. Attached on the air side of the STM system is a low noise current amplifier from Femto (DLPCA-200).²⁷ For temperature measuring and controlling a Lakeshore 340 Temperature controller²⁸ is used. The STM system was operated with two different STM controller so far. The 2H-NbSe₂ measurements were performed with the RHK SPM 100 controller²⁹ while the presented LiFeAs data were measured with the Specs Nanonis system.³⁰ In addition, we used a Stanford Research Lock-In amplifier SR830³¹ for acquiring all the spectroscopic data. Since the Nanonis system is not equipped with a V_{bias} modulation input, we used a home-build phase stable signal adder to combine the modulation signal with V_{bias} . For the capacitive coarse approach described in Sec. III we use the SR830 to modulate the V_{bias} and an Agilent 34401A multimeter³² to read V_{amp} . The analysis of the topographic data has been carried out with WSxM.³³

III. CAPACITIVE COARSE APPROACH

In order to begin the STM measurement after cleaving the crystal, the STM tip has to be moved from the maximum retracted position (tip-sample distance: ~ 20 mm) to the tunneling regime, i.e., to a tip-sample distance of a few angstroms without crashing the tip into the sample's surface. The conventional method to achieve this is to first perform an optical controlled coarse approach that brings the tip to a distance of a few μm from the surface of the sample. In the second step, an automatic approach procedure is started which is commonly implemented in most of the commercially available STM control electronics, and which is described in detail, e.g., in Ref. 34.

Since this STM system lacks an optical control or other means of measuring the absolute tip-sample distance a , an alternative method for controlling the coarse approach needs to be implemented because the exact position of the sample surface is unknown due to the cleaving process with an uncertainty of up to several mm. On the one hand, the automatic approach is too time consuming to span this initial maximal distance. On the other hand, the definition of a fixed coarse approach travel length is unreasonable because the risk of either a still too large remaining automatic approach distance or an uncontrolled tip crash is high.

A. Basic idea

The basic idea of the implemented control mechanism is to exploit the nonlinear behavior of the capacitance of the tip-sample system inside the STM body upon changing the tip-sample distance a (see Figure 7). Both the tip and the sample are conducting. From the electrostatic point of view this corresponds to a system of two electrodes with a gap in between, i.e., a capacitor. If the tip-sample distance a is changed, the geometry of the capacitor changes as well and thus its capacitance. This means that the capacitance is a measure of a . However, since the capacitance depends on the properties of

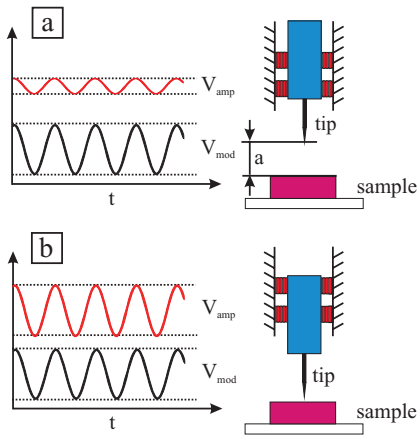


FIG. 7. Principle of a capacitive coarse approach. The signal V_{mod} is modulated on top of the sample bias V_{bias} ($V_{mod}^{pp} = 5$ V, $f_{mod} = 5000$ Hz). (a) For a large tip-sample distance a , the peak to peak (pp) value of the response signal V_{amp} is small compared to the response signal for a small sample tip distance shown in (b).

the cleaved sample and the individual geometry of the tip, it is not possible to use the capacitance directly as a threshold for the coarse approach. It is, however, possible to define a usable threshold through analyzing the apparent current that is related to the capacitance as a function of a as described in detail in the next section.

B. Analysis of the tip sample capacitor

In order to obtain an indirect measurement of the capacitance, we consider the apparent current which can be obtained from the STM current amplifier when an AC signal V_{mod} is applied to the tip-sample system, i.e., $V_{bias} = V_{mod}$. The amplifier transforms the resulting apparent current into an AC voltage signal V_{amp} , the amplitude of which depends on the impedance and thus the capacitance of the system. The qualitative dependence of V_{amp} as a function of a is illustrated in Fig. 7.

In Fig. 8 we show a representative plot of $1/V_{amp}$ which is proportional to the impedance and thus scales with the reciprocal capacitance which we measured as a function of coarse approach steps S which is proportional to a . As can be seen in Figure 8, $1/V_{amp}(S)$ possesses a positive curvature (cf. the numerical second derivative of $1/V_{amp}(S)$ shown in Fig. 8) at large distances $S \gtrsim 75 \times 10^3$. At lower distances $7.5 \times 10^3 \lesssim S \lesssim 75 \times 10^3$ the curvature is roughly zero and changes to increasingly negative values at lower S values. The onset of the negative curvature occurs at a sufficiently small a suggestive of a suitable threshold for stopping the coarse approach. We verified that the qualitative behavior shown in Fig. 8 remains unchanged for a large variety of tip-sample combinations in terms of material and geometry as well as for different temperatures. By defining a suitable negative curvature threshold value we were able to reliably find a coarse approach end position corresponding to a tip-sample distance between roughly 200 and 2000 steps, which is within reasonable reach of the short-distance automatic approach.

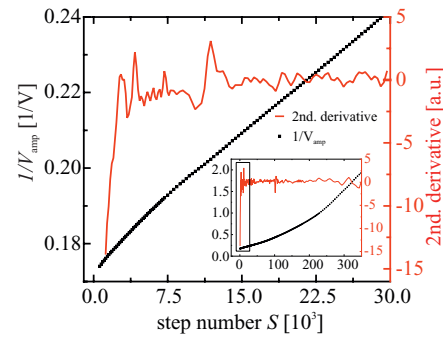


FIG. 8. Distance behavior of the tip sample capacitance. The step number S represents the distance a between tip and sample. All measured values are the peak to peak values of the amplifier signal. The inset shows the signal behavior for the whole approach range while the main plot shows the boxed region of the inset. The labels are valid for both plots. The 2nd derivative exhibits a strong decreasing behavior for small distances a . $V_{mod} = 5$ V, $f_{mod} = 5$ kHz, $1/V_{amp}$ signal (dots), and second derivative of $1/V_{amp}$ (solid line).

C. Implementation of the coarse approach

In order to exploit the afore described threshold for an automatic tip coarse approach, the curvature of $1/V_{amp}(S)$ is required to be analyzed during the coarse approach. Since the approximate measurement time for the determination of V_{amp} at a given distance is about 5 s, it is unreasonable to measure V_{amp} after each single step. Instead, such measurements will be performed only after a certain number of steps ΔS in the direction towards reduced a . Thereby it is desirable to apply a large ΔS at large a which needs to be reduced upon decreasing a , in order to prevent a tip crash. Since V_{amp} is strongly increasing during the approach, we define a voltage change threshold ΔV_{max} which describes the maximum change of V_{amp} (ΔV) between two measurements ΔS apart. If ΔV exceeds ΔV_{max} , the step number ΔS is adjusted to a suitable fraction ($\sim \frac{1}{2}$). This procedure has proven to reduce ΔS in such a way that the resolution in ΔS for numerically determining the curvature of $1/V_{amp}(S)$ is sufficiently increased to prevent a tip crash. At the same time, the required time for the coarse approach remains lower than 1-2 h.

IV. PROPERTIES

The STM system possesses several outstanding features. The liquid helium consumption at base temperature is very low (~ 1.5 l/day). Accordingly, by using, e.g., a 200 l He dewar, this corresponds to a total measurement time of about 90 days without refilling the dewar. This is a particular advantage for the performance of long-term measurements, such as large full-spectroscopy maps on a crystal surface.^{35,36} The cool down time of the STM is about 6 h (see Figure 9), where this value depends on the type of the installed thermal coupling (Figure 3(5)). The total time between mounting the sample and the first measurements on the test sample amounts ~ 10 h.

The heating cup (Figure 3(6)) allows to stabilize the STM head at any temperature between base temperature and 30 K (see Figure 10), where even higher temperatures up to room temperature are in principle possible, but have not been tested

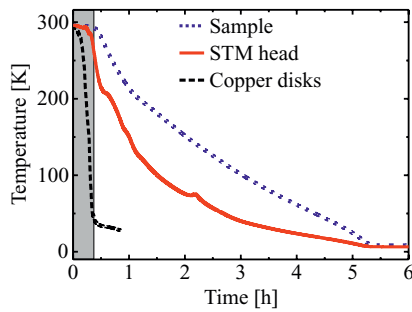


FIG. 9. Cool down behavior of the dip-stick-STM. We use the heating cup at the beginning of the cool down procedure to avoid adsorbates in the STM head. Once the copper disks reach 50 K, the heating cup is switched off. Sample sensor and STM head sensor are Cernox sensors by Lakeshore. A Pt100 sensor (Heraeus M222) is attached to the copper disks.

yet. For controlling the temperature with an external PID-controller the STM head temperature sensor (item (22) in Fig. 4) is used. The sample temperature is monitored with the sensor close to the sample holder (21).

A. Long term stability and spectroscopy

First test measurements were performed on *in situ* cleaved 2H-NbSe₂ which is ideal for calibrating the scanner. The used tip was a chemically etched³⁷ W-wire which was further improved by field emission on a gold on mica sample holder mounted on top of the cleaving post.

2H-NbSe₂ belongs to the family of the dichalcogenides and consists of selenide-niobium-selenide layers³⁸ as shown in Figure 11. This material normally cleaves in between two selenide planes. 2H-NbSe₂ undergoes a charge density wave transition (CDW) at 33.5 K.^{39,40} The CDW is commensurate with a superlattice of $3a \times 3a$ (lattice constant $a = 0.345$ nm⁴¹).

After cleaving the sample at 10 K, we resolved an atomically flat surface without any step edges (Figure 12(a)). It shows a topographic scan with atomic resolution and a clearly resolved CDW pattern.

In order to test the long-term stability of the dip-stick-STM, we measured a 128×128 spectroscopy map (Figure 13) on the 2H-NbSe₂ surface. All spectroscopy measurements were performed with the lock-in technique. The topography (Figure 13(a)) shows the atomically resolved sur-

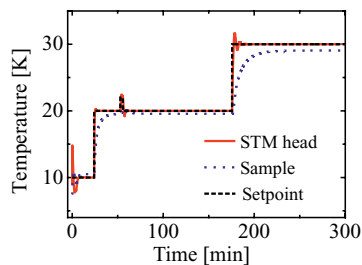


FIG. 10. Temperature behavior of the microscope. We stabilized the STM head at 10 K, 20 K, and 30 K. The stabilization time varies with temperature and is ~ 50 min at 30 K. An additional cooling by the bias wire leads to an increasing temperature difference between the sample and the STM-head. The kink at 55 min is due to changes of the setpoint.

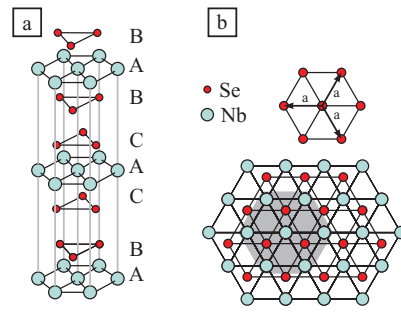


FIG. 11. (a) Crystal structure of 2H-NbSe₂ and (b) top view of NbSe₂ for half the unit cell (ABA).

face layer at the stabilization conditions of $V_{\text{bias}} = 200$ mV, $I_T = 0.7$ nA. At this bias voltage, the CDW is hard to observe. The same applies for the map of the differential conductance dI/dV at 100 mV (Figure 13(b)). In contrast, at negative bias $V_{\text{bias}} = -100$ mV the CDW is clearly visible in the differential conductance map (Figure 13(c)). Furthermore, a modulation due to the atomic lattice is resolved during the whole spectroscopic measurement which demonstrates the long term stability of the STM.

An important quantity to characterize the long-term stability is the sample drift which is caused by the inhomogeneous thermal expansion and time-dependent temperature distributions in the STM head. The drift is the decisive limiting factor for long time measurements, such as spectroscopic maps.

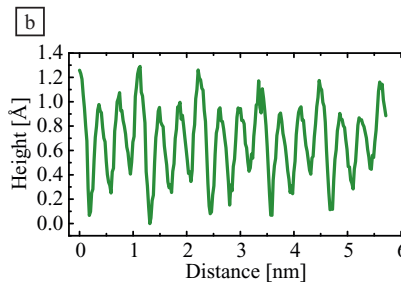
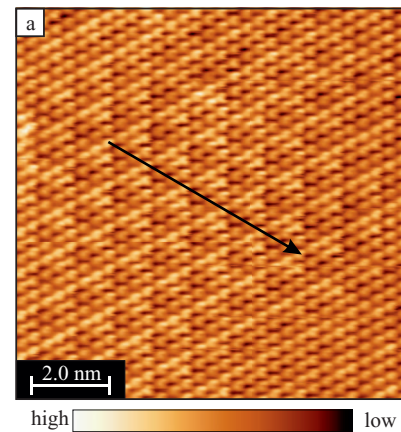


FIG. 12. (a) Constant current image of 2H-NbSe₂ (10 nm \times 10 nm), $V_{\text{bias}} = -200$ mV, $I_T = 0.7$ nA, $T = 10$ K, and $t_{\text{image}} \approx 26$ s. The topography shows the charge density wave with a periodicity of 3×3 lattice constant. (b) Line section taken along the arrow.

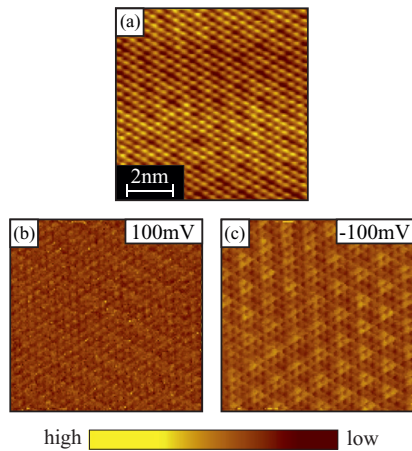


FIG. 13. 128×128 point spectroscopy map ($8 \text{ nm} \times 8 \text{ nm}$) of 2H-NbSe_2 . (a) Topography at stabilization conditions $V_{\text{bias}} = 200 \text{ mV}$, $I_T = 0.7 \text{ nA}$, $T = 10 \text{ K}$, RMS lock-in excitation $V_{\text{mod}} = 6 \text{ mV}$, $t_{\text{map}} = 16.5 \text{ h}$, spectra measured from 100 mV to -100 mV ; (b) dI/dV spectroscopic map at 100 mV ; (c) dI/dV spectroscopic map for -100 mV . The CDW pattern is hardly visible at 100 mV but clearly observable at -100 mV . The atomic structure is prominent at both voltages.

To determine the drift during the spectroscopy, we compared the measured lattice constants in the field of view shown in Figures 12 and 13 which have registered with the very different data acquisition times $t_{\text{image}} \approx 26 \text{ s}$ and $t_{\text{image}} \approx 16.5 \text{ h}$, respectively. We assume the drift during the measurement for Figure 12 being negligibly small as compared to that of the other. For determining the drift velocity, it is necessary to consider the number of atoms in one direction of the same scan area. The difference between these numbers represents the drifted distance of the sample during the measurement and results in the extraordinary small drift velocity

$$v_{\text{drift}} = 10.45 \text{ pm/h.} \quad (1)$$

This high long-term stability of the STM system allows to acquire large spectroscopic maps, which is necessary to study, e.g., atomically resolved quasiparticle interference. Corresponding examples are described in Refs. 35 and 36 which are based on data sets with a measurement time of ~ 3.5 days per map.

B. Energy resolution

In order to investigate the spectroscopic capabilities, we studied the superconducting properties of LiFeAs which is an unconventional type II superconductor with a transition temperature of 18 K .⁴² The crystal was grown as described in Ref. 43 and its structure is shown in Figure 14. The material is expected to cleave between two Li layers, where high-quality cleaved surfaces have been observed in STM with atomic resolution which allows to study the superconducting gap of the material.^{35,44,45}

For determining the energy resolution of the STM, we measured the temperature dependent dI/dV spectra on a defect free surface of a cleaved LiFeAs crystal (Figure 15). The data reveal the opening of a superconducting gap at $T \lesssim 16 \text{ K}$. Upon reducing the temperature the signatures of the gap become increasingly pronounced until a temperature of 6 K is

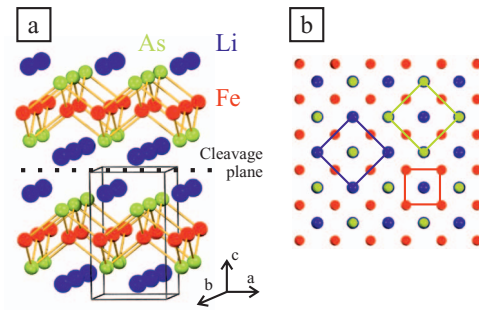


FIG. 14. Lattice structure of LiFeAs . (a) Side view: It consists of an iron layer, covalently bonded to two arsenic layers. The lithium is positioned next to the arsenic. The sample cleaving takes place in between two lithium layers. (b) Top view on the LiFeAs lattice with the drawn sub-lattices of As, Li, and Fe.

reached. At lower temperatures we do not observe further changes of the spectra down to the base temperature of 4.7 K . Therefore, we conclude that the energy resolution of the STM is $\Delta E \approx 3.5k_B T = 1.8 \text{ meV}$.

C. Thermal stability at elevated temperatures

At elevated temperature, the thermal drift increases and therefore strongly affects the STM and STS measurements. For the latter it is crucial for the tunneling junction to remain stable. This means that the relative movement of the tip versus the sample due to the thermal drift must remain negligible, because even small changes have an impact on the measured spectra. We tested the stability of the tunneling junction at the elevated temperature of 18 K by investigating the reproducibility of the measured spectra at a fixed tip position. To be specific, in Fig. 16 we compare the measured differential conductance data of LiFeAs which we obtained after stabilizing the tunnel junction at negative bias voltage and ramping V_{bias} up and down between -15 mV and 15 mV without another stabilization in between. As can be seen in Figure 16 that the two spectra are practically identical which demonstrates an extraordinary stability of the junction during the data acquisition time of $\sim 16 \text{ s}$ without the feedback loop. Furthermore, a topographic measurement which was taken at the temperature with total data acquisition time of $\sim 9 \text{ min}$ shows no

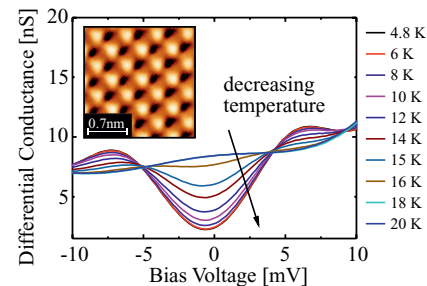


FIG. 15. Averaged spectra of LiFeAs from 6 K to 18 K . The spectra have been measured on the defect free surface shown in the inset ($2 \text{ nm} \times 2 \text{ nm}$, $V_{\text{bias}} = -35 \text{ mV}$, $I_T = 0.3 \text{ nA}$, $t_{\text{image}} = 8.5 \text{ min}$). Each temperature curve is an average of 800 curves taken on a 20×20 spectroscopic grid. Stabilization conditions: $V_{\text{bias}} = -35 \text{ mV}$, $I_T = 0.3 \text{ nA}$, RMS lock-in excitation $V_{\text{mod}} = 0.4 \text{ mV}$. The spectra show the closing of the gap with increasing temperature.

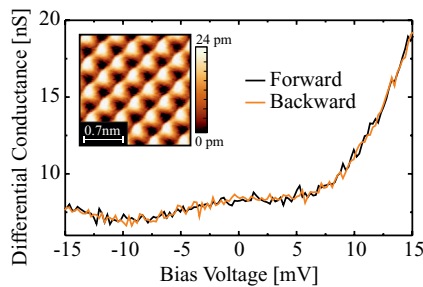


FIG. 16. Forward (V_{bias} swept from -15 mV to 15 mV) and backward (V_{bias} swept from 15 mV to -15 mV) spectra at 18 K. The spectra have been measured in one run without stabilizing after the forward spectra. Measuring time for both spectra: 16.4 s; stabilization conditions: $V_{\text{bias}} = -35$ mV, $I_T = 0.3$ nA. The spectra are located on top of each other without showing any indication of drift. Inset: Topography taken before spectroscopy. The atomically resolved image shows no indication for drift. Measurement conditions: $2 \text{ nm} \times 2 \text{ nm}$, $V_{\text{bias}} = -35$ mV, $I_T = 0.3$ nA, $T = 18$ K, $t_{\text{image}} \approx 8.7$ min.

discernible sign of a drift and confirms the high stability of the system.

D. Measurements in magnetic field

In modern condensed matter physics, the possibility to perform experimental investigation in an external magnetic field is of high importance because it allows to manipulate the ground state properties. A prominent example where such a magnetic field leads to a spatial variation of the ground state order parameter is the vortex state of a type-II superconductor. A convenient way to image the vortex lattice of a type-II superconductor is to spectroscopically map out the spatial variation of the zero bias conductance.⁴⁶ Resulting data not only provide images of the vortex lattice itself but allow in addition to extract important parameters of the superconductor such as the Ginzburg-Landau coherence length.

We performed such measurements on a LiFeAs crystal in a magnetic field of 6 T which we generated in a standard commercial bath cryostat.⁴⁷ Corresponding data are shown in Fig. 17. The core of the vortices are clearly revealed as re-

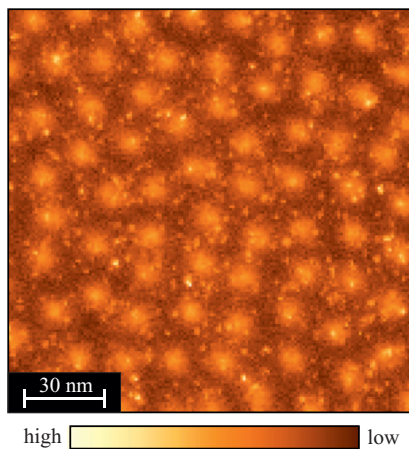


FIG. 17. Zero bias conductance at 6 T of a LiFeAs surface; spectroscopic map: $150 \text{ nm} \times 150 \text{ nm}$, 150×150 pixel, stabilization conditions: $V_{\text{bias}} = -35$ mV, $I_T = 0.3$ nA, $T = 6$ K, $B = 6$ T, $t_{\text{map}} = 34$ h. The large bright spots show the vortex lattice of LiFeAs where the small spots represent defects on the surface. The vortex lattice itself can be described as a vortex glass.

gions with an enhanced zero bias conductance. Interestingly, the lattice differs from the classical Abrikosov lattice⁴⁸ but resembles a vortex glass⁴⁹ consistent with previous results published by Hanaguri *et al.*⁴⁴ Thus, the operation of the STM in magnetic field is clearly demonstrated.

V. SUMMARY

We presented the design and the characterization of a compact cryogenic STM which operates in the temperature range between 4.7 K and room temperature. Its special design possesses the flexibility to operate it either in a standard transport dewar of liquid ^4He or in a commercial magnet bath cryostat. The system exhibits an outstanding low liquid helium consumption of 1.5 l/day which allows for long-term measurements without refilling of up to 90 days, and the application of high magnetic fields (up to ~ 18 T). A cryogenic cleaving stage allows to cleave single crystalline samples in cryogenic vacuum conditions at base temperature prior to actual STM measurements for preparing atomically flat clean surfaces. Furthermore, we described a solution for an automatic coarse approach without optical access. During test measurements on 2H-NbSe_2 and LiFeAs, the system demonstrated a remarkable performance and stability at various temperatures and in magnetic fields.

ACKNOWLEDGMENTS

The authors thank the mechanical and electrical workshop of the IFW Dresden for helpful technical discussions and machining most parts of the STM and F. Herold for building the frame. This work was supported by the Deutsche Forschungsgemeinschaft through SPP 1458 (Grant No. HE 3439/11), FOR 1154 (Grant No. HA6037/1), and through GRK 1621.

- ¹M. F. Crommie, C. P. Lutz, and D. M. Eigler, *Nature* **363**, 524 (1993).
- ²L. Petersen, P. T. Sprunger, P. Hofmann, E. Lægsgaard, B. G. Briner, M. Doering, H.-P. Rust, A. M. Bradshaw, F. Besenbacher, and E. W. Plummer, *Phys. Rev. B* **57**, R6858 (1998).
- ³J. E. Hoffman, K. McElroy, D.-H. Lee, K. M. Lang, H. Eisaki, S. Uchida, and J. C. Davis, *Science* **297**, 1148 (2002).
- ⁴T. Hanaguri, Y. Kohsaka, M. Ono, M. Maltseva, P. Coleman, I. Yamada, M. Azuma, M. Takano, K. Ohishi, and H. Takagi, *Science* **323**, 923 (2009).
- ⁵C. V. Parker, P. Aynajian, E. H. da Silva Neto, A. Pushp, S. Ono, J. Wen, Z. Xu, G. Gu, and A. Yazdani, *Nature* **468**, 677 (2010).
- ⁶O. Fischer, M. Kugler, I. Maggio-Aprile, C. Berthod, and C. Renner, *Rev. Mod. Phys.* **79**, 353 (2007).
- ⁷P. Roushan, J. Seo, C. V. Parker, Y. S. Hor, D. Hsieh, D. Qian, A. Richardella, M. Z. Hasan, R. J. Cava, and A. Yazdani, *Nature* **460**, 1106 (2009).
- ⁸J. Seo, P. Roushan, H. Beidenkopf, Y. S. Hor, R. J. Cava, and A. Yazdani, *Nature* **466**, 343 (2010).
- ⁹A. J. Heinrich, J. A. Gupta, C. P. Lutz, and D. M. Eigler, *Science* **306**, 466 (2004).
- ¹⁰S. Loth, S. Baumann, C. P. Lutz, D. M. Eigler, and A. J. Heinrich, *Science* **335**, 196 (2012).
- ¹¹S. Loth, M. Etzkorn, C. P. Lutz, D. M. Eigler, and A. J. Heinrich, *Science* **329**, 1628 (2010).
- ¹²A. A. Khajetoorians, B. Baxevanis, C. Hübner, T. Schlenk, S. Krause, T. O. Wehling, S. Lounis, A. Lichtenstein, D. Pfannkuche, J. Wiebe, and R. Wiesendanger, *Science* **339**, 55 (2013).
- ¹³P. Bedrossian and T. Klitsner, *Phys. Rev. B* **44**, 13783 (1991).
- ¹⁴J. J. R. Arthur, *J. Appl. Phys.* **39**, 4032 (1968).

- ¹⁵R. A. Hughes, Y. Lu, T. Timusk, and J. S. Preston, *Appl. Phys. Lett.* **58**, 762 (1991).
- ¹⁶K. Jousten, *Wutz Handbuch Vakuumtechnik*, 9th ed. (Vieweg, 2006).
- ¹⁷*Kompaktzylinder Unitop*, Fa. Riegler and Co. KG, Schuetzenstraße 27, D-72574 Bad Urach, Germany.
- ¹⁸*Bilz Faebi Rubber Air Springs*, BILZ Vibration Technology AG, BILZ Vibration Technology AG, Böblinger Straße 25, D-71229 Leonberg, Germany.
- ¹⁹*Macor*, Corning Incorporated, One Riverfront Plaza Corning, New York 14831, USA.
- ²⁰*Lake Shore Cryotronics, Cernox Sensor*, Lake Shore Cryotronics, Inc., 575 McCorkle Blvd, Westerville, Ohio 43082-8699, USA.
- ²¹S. H. Pan, "Piezo-electric motor," International Patent Publication Number WO 93/19494 (International Bureau, World Intellectual Property Organization, 1993).
- ²²*EBL Piezo Electric Ceramics*, EBL Products Inc., 91 Prestige Park Circle, East Hartford, Connecticut, 06108, USA.
- ²³*Epotek H20E Epoxy Glue*, Epoxy Technology, Inc., 14 Fortune Drive, Billerica, Massachusetts 01821-3972, USA.
- ²⁴G. Mariotto, M. D. Angelo, and I. V. Shvets, *Rev. Sci. Instrum.* **70**, 3651 (1999).
- ²⁵*Epotek H70E Epoxy Glue*, Epoxy Technology, Inc., 14 Fortune Drive, Billerica, Massachusetts 01821-3972, USA.
- ²⁶H. B. J. Wintterlin, J. Wiechers, and T. Gritsch, *Phys. Rev. Lett.* **62**, 59 (1989).
- ²⁷*Femto, Amplifier DLCPA-200*, FEMTO Messtechnik GmbH, Klosterstraße 64, D-10179 Berlin, Germany.
- ²⁸*Lake Shore Cryotronics, Temp. Controller 340*, Lake Shore Cryotronics, Inc., 575 McCorkle Blvd, Westerville, Ohio 43082-8699, USA.
- ²⁹*RHK, SPM Controller*, RHK Technology, Inc., 1050 East Maple Road Troy, Michigan 48083, USA.
- ³⁰*Specs, Nanonis SPM Controller*, SPECS Surface Nano Analysis GmbH, Voltastraße 5, D-13355 Berlin, Germany.
- ³¹*Stanford Research, SR830*, Stanford Research Systems, Inc., 1290-D Reamwood Avenue, Sunnyvale, California 94089, USA.
- ³²*Agilent Technologies, 34401*, Agilent Technologies, Inc., 5301 Stevens Creek Blvd, Santa Clara, California 95051, USA.
- ³³I. Horcas, R. Fernandez, J. M. Gomez-Rodriguez, J. Colchero, J. Gomez-Herrero, and A. M. Baro, *Rev. Sci. Instrum.* **78**, 013705 (2007).
- ³⁴C. J. Chen, *Introduction to Scanning Tunneling Microscopy*, 2nd ed. (Oxford University Press, 2008).
- ³⁵T. Hänke, S. Sykora, R. Schlegel, D. Baumann, L. Harnagea, S. Wurmehl, M. Daghofer, B. Büchner, J. van den Brink, and C. Hess, *Phys. Rev. Lett.* **108**, 127001 (2012).
- ³⁶C. Hess, S. Sykora, T. Hänke, R. Schlegel, D. Baumann, V. B. Zabolotnyy, L. Harnagea, S. Wurmehl, J. van den Brink, and B. Büchner, *Phys. Rev. Lett.* **110**, 017006 (2013).
- ³⁷J. P. Ibe, P. P. Bey, S. L. Brandow, R. A. Brizzolara, N. A. Burnham, D. P. DiLella, K. P. Lee, C. R. K. Marrian, and R. J. Colton, *J. Vac. Sci. Technol.* **8**, 3570 (1990).
- ³⁸J. A. Wilson and A. D. Yoffe, *Adv. Phys.* **18**, 193 (1969).
- ³⁹D. E. Moncton, J. D. Axe, and F. J. D. Salvo, *Phys. Rev. Lett.* **34**, 734 (1975).
- ⁴⁰G. Grüner, *Rev. Mod. Phys.* **60**, 1129 (1988).
- ⁴¹B. E. Brown and D. J. Beernten, *Acta Cryst.* **18**, 31 (1965).
- ⁴²J. H. Tapp, Z. Tang, B. Lv, K. Sasmal, B. Lorenz, P. C. W. Chu, and A. M. Guloy, *Phys. Rev. B* **78**, 060505 (2008).
- ⁴³I. Morozov, A. Boltalin, O. Volkova, A. Vasiliev, O. Kataeva, U. Stockert, M. Abdel-Hafiez, D. Bombor, A. Bachmann, L. Harnagea, M. Fuchs, H.-J. Grafe, G. Behr, R. Klingeler, S. Borisenko, C. Hess, S. Wurmehl, and B. Büchner, *Cryst. Growth Des.* **10**, 4428 (2010).
- ⁴⁴T. Hanaguri, K. Kitagawa, K. Matsubayashi, Y. Mazaki, Y. Uwatoko, and H. Takagi, *Phys. Rev. B* **85**, 214505 (2012).
- ⁴⁵S. Grothe, S. Chi, P. Dosanjh, R. Liang, W. N. Hardy, S. A. Burke, D. A. Bonn, and Y. Pennec, *Phys. Rev. B* **86**, 174503 (2012).
- ⁴⁶M. R. Eskildsen, M. Kugler, S. Tanaka, J. Jun, S. Kazakov, J. Karpinski, and Ø. Fischer, *Phys. Rev. Lett.* **89**, 187003 (2002).
- ⁴⁷*Oxford Instruments, ⁴He-Cryostat*, Oxford Instruments PLC, Tubney Woods Abingdon, Oxfordshire OX13 5QX, United Kingdom.
- ⁴⁸A. A. Abrikosov, *Sov. Phys. JETP* **5**, 1174 (1957).
- ⁴⁹G. Blatter, *Phys. C* **282–287**(Part 1), 19 (1997).